International Journal of Nanomedicine

Dovepress
open access to scientific and medical research

Open Access Full Text Article

ORIGINAL RESEARCH

Near Infrared-Activatable Biomimetic Nanoplatform for Tumor-Specific Drug Release, Penetration and Chemo-Photothermal Synergistic Therapy of Orthotopic Glioblastoma

Ming Li*, Xinrui Zhang*, Yujie Zhou, Yuteng Chu, Jie Shen, Yue Cai, Xuanrong Sun

Collaborative Innovation Center of Yangtze River Delta Region Green Pharmaceuticals, Zhejiang University of Technology, Hangzhou, 310014, People's Republic of China

*These authors contributed equally to this work

Correspondence: Xuanrong Sun, Collaborative Innovation Center of Yangtze River Delta Region Green Pharmaceuticals, Zhejiang University of Technology, Hangzhou, 310014, People's Republic of China, Email sunxr@zjut.edu.cn

Introduction: Glioblastoma multiforme (GBM), a highly invasive and prognostically challenging brain cancer, poses a significant hurdle for current treatments due to the existence of the blood-brain barrier (BBB) and the difficulty to maintain an effective drug accumulation in deep GBM lesions.

Methods: We present a biomimetic nanoplatform with angiopep-2-modified macrophage membrane, loaded with indocyanine green (ICG) templated self-assembly of SN38 (AM-NP), facilitating active tumor targeting and effective blood-brain barrier penetration through specific ligand-receptor interaction.

Results: Upon accumulation at tumor sites, these nanoparticles achieved high drug concentrations. Subsequent combination of laser irradiation and release of chemotherapy agent SN38 induced a synergistic chemo-photothermal therapy. Compared to bare nanoparticles (NPs) lacking cell membrane encapsulation, AM-NPs significantly suppressed tumor growth, markedly enhanced survival rates, and exhibited excellent biocompatibility with minimal side effects.

Conclusion: This NIR-activatable biomimetic camouflaging macrophage membrane-based nanoparticles enhanced drug delivery targeting ability through modifications of macrophage membranes and specific ligands. It simultaneously achieved synergistic chemo-photothermal therapy, enhancing treatment effectiveness. Compared to traditional treatment modalities, it provided a precise, efficient, and synergistic method that might have contributed to advancements in glioblastoma therapy.

Keywords: biomimetic macrophage membrane, drug delivery, synergistic treatment, glioma inhibition, near infrared-activatable

Introduction

Glioblastoma multiforme (GBM) is recognized as one of the most prevalent primary brain cancers, exhibiting high invasiveness and often manifesting in critical regions of the brain, resulting in a disheartening five-year survival rate of less than 5%.[1–3] The formidable challenge of achieving complete surgical excision of GBM through current medical techniques necessitates a critical exploration of alternative treatment paradigms. Notably, the prevalent therapeutic approach involves a combination of radiotherapy and chemotherapy;[4] however, this combined modality yields poor prognosis and falls short of delivering anticipated therapeutic efficacy to patients.[5–7]

In particular, to approach effective drug concentrations in the GBM lesions, which is highly desired for optimal therapeutic outcomes, suffer from fast clearance by the reticuloendothelial (RES) system,[8,9] limited BBB penetration,[10,11] and insufficient tumor uptake.[12,13] Efficient delivery of intravenously administered therapeutics across the BBB and other biological barriers into the deep tumor remains an insurmountable challenge for GBM treatment.[14]

Received: 28 February 2024
Accepted: 3 July 2024
Published: 11 July 2024

Integrating multiple treatment modalities has been considered revolutionary strategies in overcoming a series of biological barriers for anticancer treatment.[15,16] Nevertheless, the formidable barrier presented by the BBB significantly hampers the efficiency of drug delivery to the brain, thereby undermining GBM's treatment efficacy.[17,18] Although interventions such as ultrasound[19–21] or mechanical means[22,23] can transiently open the BBB, they simultaneously pose a risk of introducing deleterious substances into the brain. Therefore, functional nanoparticles have emerged as promising carriers for BBB penetration, as they can encapsulate therapeutic agents, shield them from enzymatic degradation, and facilitate targeted delivery to the brain parenchyma. They rely on safe natural cells as carriers, such as natural cells,[24,25] extracellular vesicles,[26–28] and biological membranes[29,30], and undergo various surface modifications to interact with BBB endothelial cells, promoting transcytosis and bypassing efflux transporters that typically hinder drug permeation. Muhammad Ismail et al achieved effective BBB penetration using functionalized red blood cell membrane camouflage, significantly inhibiting the growth of glioblastoma[31] but still, infiltration from blood vessels into GBM tumor tissue and to distal tumor cells remains largely inefficient for bulk nanoparticles. Precisely activatable drug delivery nanoplatforms are therefore highly desired to warrant efficient BBB penetration and tumor-specific release of therapeutic agents for successful GBM treatment.[32,33]

In this study, as illustrated in Scheme 1, we utilized a naturally derived macrophage membrane to encapsulate nanoparticles formed by self-assembly of indocyanine green (ICG) and SN38 and to further enhance the targeting effect by surface modification of Angiopep-2, creating a nanoplatform capable of actively targeting glioblastomas and achieving chemo-photothermal synergistic therapy. ICG is a photosensitizer capable of generating heat when exposed to 808 nm laser, making it pivotal in photothermal applications. SN38, derived from the active metabolism of CPT-11, functions by inhibiting topoisomerase I, thereby impeding cancer cell proliferation. However, these agents often exhibit poor stability in vivo, necessitating modifications to enhance therapeutic efficacy while minimizing adverse effects.[34] The Angiopep-2 peptide, known for its affinity for low-density lipoprotein receptors, facilitates BBB penetration,[35–37] while

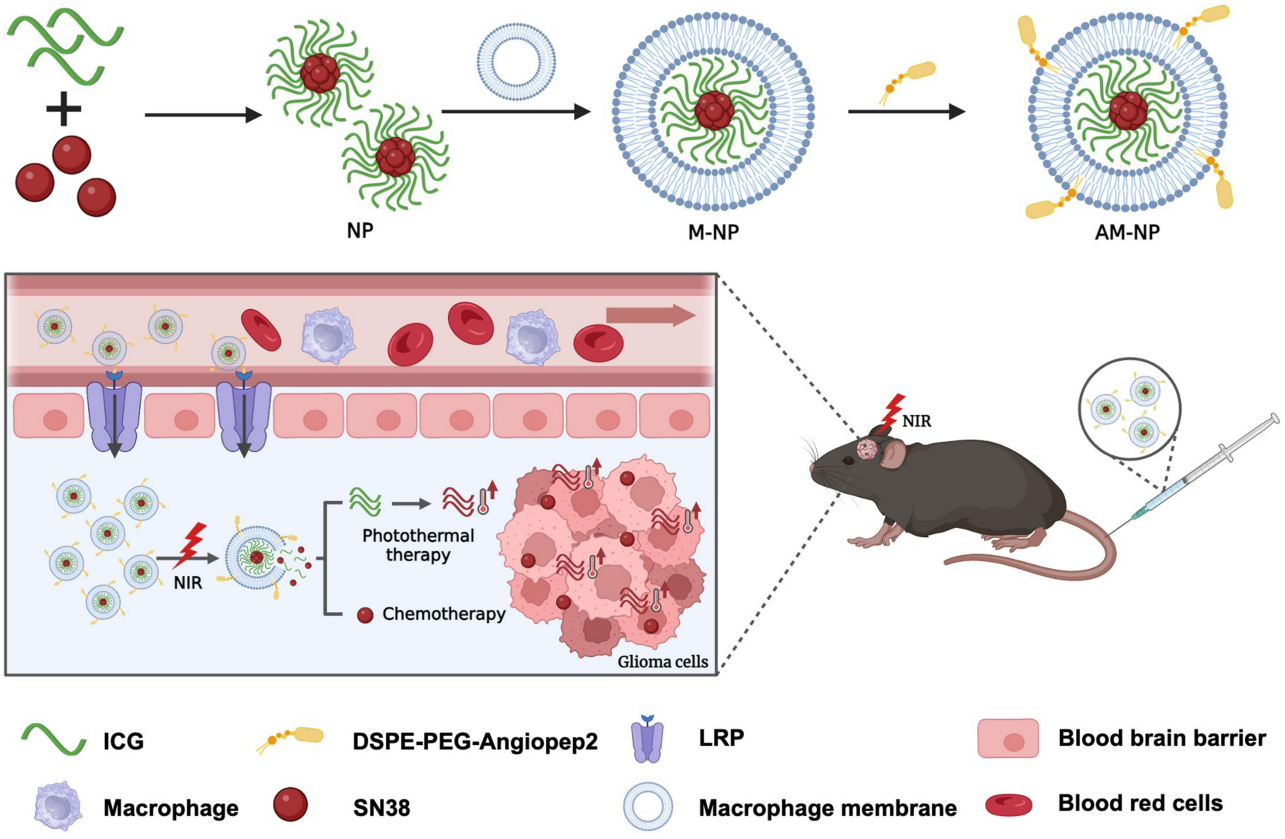

Scheme 1 Scheme of illustration of the preparation process of nanoparticles and their utilization in synergistic chemical-photothermal therapy (Created with BioRender.com).

the macrophage membrane specifically targets integrin receptors abundantly expressed on the surfaces of glioblastoma and brain vascular endothelial cells, simultaneously evade clearance and enhance drug accumulation.[38–40] Thus, the developed drug delivery system achieves dual-targeting of glioblastomas and brain vascular endothelial cells. Upon reaching the tumor site and subsequent exposure to 808 nm laser irradiation, ICG induces effective hyperthermia,[41,42] facilitating localized thermal therapy and triggering the burst release of SN38. The released SN38, by inhibiting DNA topoisomerase, induces tumor cells apoptosis, thereby realizing the synergistic effects of chemo-photothermal therapy. This refined strategy not only leverages the potential of natural cellular components but also highlights the importance of effective drug retention and a diversified treatment paradigm, contributing to the ongoing pursuit of an optimal treatment approach for GBM.

Materials and Methods

Materials

Angiopep-2-cys (TFFYGGSRGKRNNFKTEEYC) with purity ≥ 95% were purchased from ChinaPeptides Co., Ltd (Shanghai, China). DSPE-PEG_{2000}-Mal was provided by Ruixi Biological Technology Co., Ltd (Xi'an, China). Indocyanine Green (ICG, CAS:3599-32-4) and 7-Ethyl-10-hydroxycamptothecin (SN38, CAS:86639-52-3) were purchased from Aladdin Bio-Chem Technology Co., Ltd (Shanghai, China). DMEM and DMEM/F12 cell culture medium, penicillin/streptomycin stock solutions, fetal bovine serum (FBS) and trypsin were all purchased from Gibco BRL (Gaithersburg, MD, USA). The membrane protein extraction kit (Product number: P0033) was purchased from beyotime (Shanghai, China). The Rabbit Anti-Calreticulin antibody (Product number: bs-5913R) and Goat Anti-Rabbit IgG H&L/AF488 antibody (Product number: bs-0295g-AF488) were purchased from Bioss (Beijing, China).

Cells and Animals

RAW264.7, bEnd.3, and GL261 cells were all obtained from the China Center for Type Culture Collection (Wuhan, China). RAW264.7 and bEnd.3 cells were cultured in DMEM containing 10% FBS and 1% antibiotics (Penicillin/Streptomycin), while GL261 cells were cultured in DMEM/F12 containing 10% FBS and 1% antibiotics (Penicillin/Streptomycin).

6-week-old female ICR mice (weighing 18–22 g) and C57BL/6 mice (4–5 weeks old, weighing 14–16 g) were procured from Shanghai Slac Laboratory Animal Co. Ltd.

Synthesis of DSPE-PEG-Angiopep-2

To synthesize DEPE-PEG-Angiopep-2, 5 mg of DSPE-PEG-Mal was completely dissolved in 10 mL of water. Then, 6 mg of Angiopep-2-cys was added to the solution, and the mixture was stirred at 37°C for 12 hours. The solution was dialyzed (MW3500) to remove excess Angiopep-2-cys. The resulting purified product, DSPE-PEG-Angiopep-2, was then freeze-dried and stored at −20°C for subsequent usage.

Isolation of Macrophage Membrane

RAW264.7 cells were suspended at a density of 2.5×10^7 cells·mL^{-1} in ice-cold TM buffer solution (pH 7.4; 10 mM Tris + 1 mM $MgCl_2$). Subsequently, cells' disruption was achieved by ultrasonication for 5 min under ice-bath conditions. 1 M sucrose was subsequently mixed with the cell homogenate to eventually reach 0.25 M sucrose concentration, and the mixture was centrifuged at 2000 g and 4°C for approximately 10 min. The resulting supernatant was subject for collection upon further centrifugation at 3000 g for an additional 30 min.[43] The cell membranes were collected and washed with ice-cold TM buffer in the presence of 0.25 M of sucrose twice for purification.[44] Subsequently, the membrane protein content was measured by BCA protein assay to be approximately 0.25 mg per 30 million cells. The extracted macrophage membranes were then stored at −20°C for preservation.

Preparation of NP, M-NP and AM-NP

ICG/SN-38 nanoparticle (NP) was prepared as previously reported with modification.[45] Briefly, 1 mg ICG and 1 mg SN-38 were dissolved in 20 μL DMSO, then 1 mL water was added into the solution followed by 5 min ultrasonication. The formulation was dialyzed (MW3500) against distilled water (1 L) for 12 h. Then, an ultrasound of the NP solution with a certain amount of macrophage membrane for 2 min to obtain macrophage membrane/ICG/SN-38 (M-NP). Furthermore, 1 mL Angiopep-2 decorated M-NP (AM-NP) was obtained by sonication (400 W, 2 s on/ 3 s off, 2 min) of M-NP and 100 μg DSPE-PEG-Angiopep-2 previously prepared.

Characterization of NP, M-NP and AM-NP

The assessment of nanoparticle dimensions and zeta potential was conducted through the utilization of a dynamic light scattering (DLS) detector (Zetasizer, Nano-ZS90, Malvern, UK) at a temperature of 25°C. The stability of the nanoparticles was subsequently evaluated over a span of 3 days in both fetal bovine serum (FBS) and phosphate-buffered saline (PBS) with a pH of 7.4. The morphological characterization of the nanoparticles was undertaken employing a JEM-1200EX transmission electron microscope manufactured by Jeol Ltd, Japan.

The drug release assay for SN38 was conducted using the dialysis method under different pH conditions. Specifically, 1 mL of AM-NP formulation containing 0.08 mg of SN38 was loaded into a dialysis bag (MWCO = 3500 Da) and immersed in 29 mL of PBS (pH 7.4 and 5.5) at 37°C with stirring at 180 rpm for 36 h. In the pH5.5+L group, the nanoparticles were exposed to laser irradiation for 5 min at 808 nm and 1.5 W/cm² before release. At various time points, 1 mL of PBS containing the released drug was withdrawn, and an equal volume of fresh PBS was added. The content of SN38 in the samples was determined using high-performance liquid chromatography (HPLC).

Verification of the Composition of Membrane Proteins

The prepared M-NP and AM-NP were centrifuged at 4°C and 15000 g for 10 min to obtain nanoscale precipitates. The cellular membrane proteins in M-NP and AM-NP were extracted using a membrane protein extraction kit. The extracted membrane proteins were then subjected to SDS-PAGE gel electrophoresis to assess whether there were any changes in the composition of macrophage membrane proteins on the nanoparticles.[46]

In vitro Cytotoxicity Studies

The antitumor efficacy of nanoparticles was evaluated through the implementation of MTT assay in this study. GL261 cells were seeded on a 96-well plate at a density of 5×10^3 cells/well for 12 h. The cells were exposed to serial dilutions of SN38, NP, M-NP, AM-NP and free ICG with or without irradiation by an 808 nm laser at the power density of 1 $W\cdot cm^{-2}$ for 5 min. After 24 h of incubation, each well was treated with culture medium containing MTT, followed by a 4 h' incubation period. Subsequently, the MTT-containing medium was aspirated, and 100 μL of DMSO was added to each well. Absorbance at 570 nm was measured using a multi-functional microplate reader.

In vitro Cellular Uptake

GL261 cells were seeded at a density of 1×10^5 cells per well in 12 well plates and cultured overnight. Then different ICG formulations were added (ICG equivalent to 5 $\mu g\cdot mL^{-1}$). After 1 h of incubation, the cells were rinsed three times with PBS, then fixed with 4% paraformaldehyde for 15 min. 5 $\mu g\cdot mL^{-1}$ of Hoechst 33342 was used to stain the cell nucleus for 10 min, and finally observed under a fluorescence microscope.

Similarly, to further quantify the uptake of the nanoparticles by the cells, the cells were collected for flow cytometry analysis after 1 h of incubation with different nanoparticles.

Moreover, to confirm Angiopep-2 peptide-mediated cellular uptake, cells were pre-treated with or without Angiopep-2 at a concentration of 500 μg/mL for 2 h before incubation of different kinds of nanoparticles, followed by observation under a fluorescence microscope.

To investigate the potential of macrophage membrane modification to facilitate nanoparticle evasion from immune cell clearance, RAW264.7 cells were cultured overnight in 12-well plates, and then incubated with NP and macrophage AM-NP at the same concentration for 2 h, followed by observation under a fluorescence microscope.

Inhibition and Penetration of Nanoparticles into Tumor Spheroids

Add 50 μL of autoclaved 1.5% agarose solution to each well of a 96-well plate. GL261 cells are then diluted in DMEM containing 0.24% methylcellulose at a density of 5×10^4 cells per mL. Subsequently, place the above cell-containing DMEM at 20 μL drops per drop on a 10 cm^2 cell culture dish lid. After overnight incubation, the spheroids were transferred to a 96-well plate pre-treated with agarose, and after 3 days of incubation, multicellular tumor spheroids of about 300 μm in diameter were obtained. Spheroids were then treated with an equal concentration of nanoparticles in which the laser-treated group was irradiated with an 808 nm laser 8 h after treatment. Tumor spheroids are recorded daily.

The GL261 spheroids were prepared as described above. The spheroids were treated with NP, M-NP and AM-NP (ICG equivalent to 10 $\mu g\cdot mL^{-1}$) to study the penetration capacity of nanoparticles. After 4 h of incubation, 4% paraformaldehyde was used to fix the tumor spheroids and then the level of permeability of nanoparticles was analyzed by using laser scanning confocal microscopy (CLSM, Nikon-AX, Japan).

In vitro Blood-Brain Barrier Permeability Assay

BEnd.3 cells were utilized to establish an in vitro BBB model.[47] Specifically, 5×10^5 bEnd.3 cells in 200 μL were seeded onto the upper chamber of a transwell plate. The lower chamber was filled with 1 mL of DMEM/F12 medium, and the medium was refreshed every two days. The resistance between the upper and lower chambers was measured using a cell resistance meter until a stable resistance was reached. Additionally, the upper chamber medium was considered successfully maintained if there was a minimal decrease within 4 h. This criterion indicated the successful preparation of the BBB model.[46]

For the in vitro BBB penetration assay, different nanomaterial formulations containing 10 $\mu g\cdot mL^{-1}$ in 200 μL were added to the upper chamber, while 500 μL of PBS solution was added to the lower chamber. After 4 h, the lower chamber solution was collected for indocyanine green (ICG) concentration determination, assessing the penetration capability of various nanomaterial formulations through the BBB.

Cellular Uptake Pathways and Subcellular Distribution

To identify the endocytic pathways involved in BBB penetration, bEnd.3 cells were cultured overnight in 12-well plates. Then, cells were separately pretreated with Nystatin (10 $\mu g\cdot mL^{-1}$, caveolin inhibitor), Chlorpromazine (10 $\mu g\cdot mL^{-1}$, clathrin inhibitor), and Amiloride (50 $\mu g\cdot mL^{-1}$, macropinocytosis inhibitor) for 30 min, along with an untreated control group. Subsequently, bEnd.3 cells were incubated with AM-NP for 4 h, and then collected for quantitative analysis using flow cytometry.

Moreover, after a certain period of incubation with AM-NP, bEnd.3 cells were treated with 50 nM Lysotracker at 37°C for 40 min to label lysosomes. After washing with PBS three times, cells were stained with 5 $\mu g\cdot mL^{-1}$ Hoechst 33342 for 10 min to label the nuclei. Subsequently, the cellular colocalization was observed under a confocal microscope.

Induction of Immunologic Cell Death (ICD)

To investigate the photothermal effect of formulations on the induction of immunogenic cell death (ICD) in tumor cells, ATP secretion and calreticulin (CRT) exposure were assessed. In brief, GL261 cells were cultured overnight in 12-well plates and treated with AM-NP, AM-NP+Laser, and ICG+Laser. After 8 h treatment, the laser-treated group underwent 5 min of laser irradiation (808 nm, 1.5 $w\cdot cm^{-2}$). Following overnight incubation, the supernatant was collected the next day for ATP measurement using an ATP assay kit.

For CRT exposure detection, cells treated under different conditions were first fixed with 4% paraformaldehyde at room temperature for 20 min. Subsequently, they were washed three times with PBS, incubated with the Calreticulin antibody at 37°C for 1 h, washed again and then incubated with Alexa 488-conjugated secondary antibody for 0.5 h. After another three washes with PBS, the cells were stained with Hoechst 33342 for 10 min to label the nuclei. The externalization of CRT was observed under a fluorescence microscope.

In vivo Pharmacokinetic Evaluation

Female ICR mice (≈20 g) were divided into three groups of six and injected with CPT-11 injection (the first-line chemotherapeutic drug, the original form of SN-38), NP, and AM-NP (an equivalent SN38 dose: 5 $mg \cdot kg^{-1}$) via the tail vein. At appropriate time intervals, 100 μL of fresh blood was collected and put in 1.5 mL tubes containing heparin sodium, and immediately centrifuged at 5000 rpm, 4°C for 10 min. After centrifugation, the supernatant was stored at −20°C. Before HPLC analysis, 50 μL of the serum was mixed with 100 μL of acetonitrile to extract SN38 and precipitate the proteins. The mixture was centrifuged at 12000 rpm, at 4°C for 10 min and the supernatant was filtered via a 220 nm filter and collected. Finally, 20 μL of the sample was tested by HPLC using acetonitrile and ultrapure water (20: 80 v/v) as the mobile phase (flow rate: 1 $mL \cdot min^{-1}$; detection wavelength: 360 nm).

In vivo Therapeutic Efficacy Study

This assay designated the central region of the right striatum in mice as the site for tumor cell inoculation.[46,48] Thirty-two female C57BL/6 mice were utilized to establish a glioma model. In short, each mouse received 5 μL of GL261 cell suspension in sterile PBS for injection. The injection site was located 1 mm posterior, 2 mm lateral to the bregma, and 3 mm ventral, with a slow injection rate of 1 $\mu L \cdot min^{-1}$ over a duration of 5 min. This resulted in the in-situ implantation of 5×10^5 tumor cells in each mouse's brain. Following the injection, the needle was left in place for 5 min before being slowly retracted. The mice were weighed and randomly divided into four groups: PBS, NP, AM-NP, AM-NP with laser. The NIR irradiation was performed at 8 h after injection (808 nm, 1.5 $W \cdot cm^{-2}$, 5 min). During the treatment period, daily monitoring of mouse body weight was conducted, and survival curves for each group were generated. After the completion of three treatment cycles, two mice from each group were randomly euthanized. Their brain tissues were extracted and washed twice in PBS buffer. The washed brain tissues were then immersed in a 4% paraformaldehyde solution and fixed overnight at 4°C. Following fixation, the brain tissues were dehydrated, embedded in paraffin, and sectioned coronally into 5 μm thick slices using a microtome. These slices were stained with hematoxylin and eosin (H&E), and the pathological condition of the brain tissues post-staining was observed under a microscope. Similarly, organs such as heart, liver, spleen, lungs, and kidneys were processed into paraffin blocks and sectioned for H&E staining to evaluate biosafety.

In vivo Brain Tumor Targeting Ability Evaluation

To assess the distribution of the drug in different tissues and the fluorescence intensity of the drug at the brain tumor site. On the tenth day after tumor inoculation in mice, mice with successful tumor modeling were selected. Subsequently, mice were intravenously injected via the tail vein with NPs and AM-NPs at different concentrations. In vivo, imaging was performed at 2 h to observe the targeting ability of different nanoformulations towards brain tumors. Mice were euthanized 8 h post-injection, and the entire brain, heart, liver, spleen, lungs, and kidneys were carefully extracted for ex vivo imaging.

Statistical Analysis

All data are presented as Mean ± SD. One-way analysis of variance (ANOVA) was used to compare differences among various groups, and *t*-tests were conducted to determine whether there were significant differences between two groups. Statistical significance was indicated as follows: *p < 0.05, **p < 0.01, ***p < 0.001, ****p < 0.0001. The more asterisks present, the more significant the difference.

Results and Discussion

Characterization of Nanoparticles

As shown in Figure 1A and B, the self-assembled nanoparticles (NPs) exhibited an average diameter of approximately 112.1±1.2 nm, with a surface zeta potential of about −14.9±0.2 mV. The subsequent preparation of M-NP and AM-NP in a slight increase in their respective diameters to 129.5±3.9 nm and 143.8±1.6 nm, with potentials of −27.2±1.6 mV and −28±1.8 mV, The encapsulation efficiencies of ICG and SN38 in the final prepared AM-NP were 73.4 ± 2.1% and 82.0 ± 2.6% with unchanged optical properties of ICG (Figures S1 and S2). For the drug-unloaded macrophage membrane (M), the measured diameter and potential are 166.3±1.3 nm and −24.1±1.5 mV, with a measured membrane protein

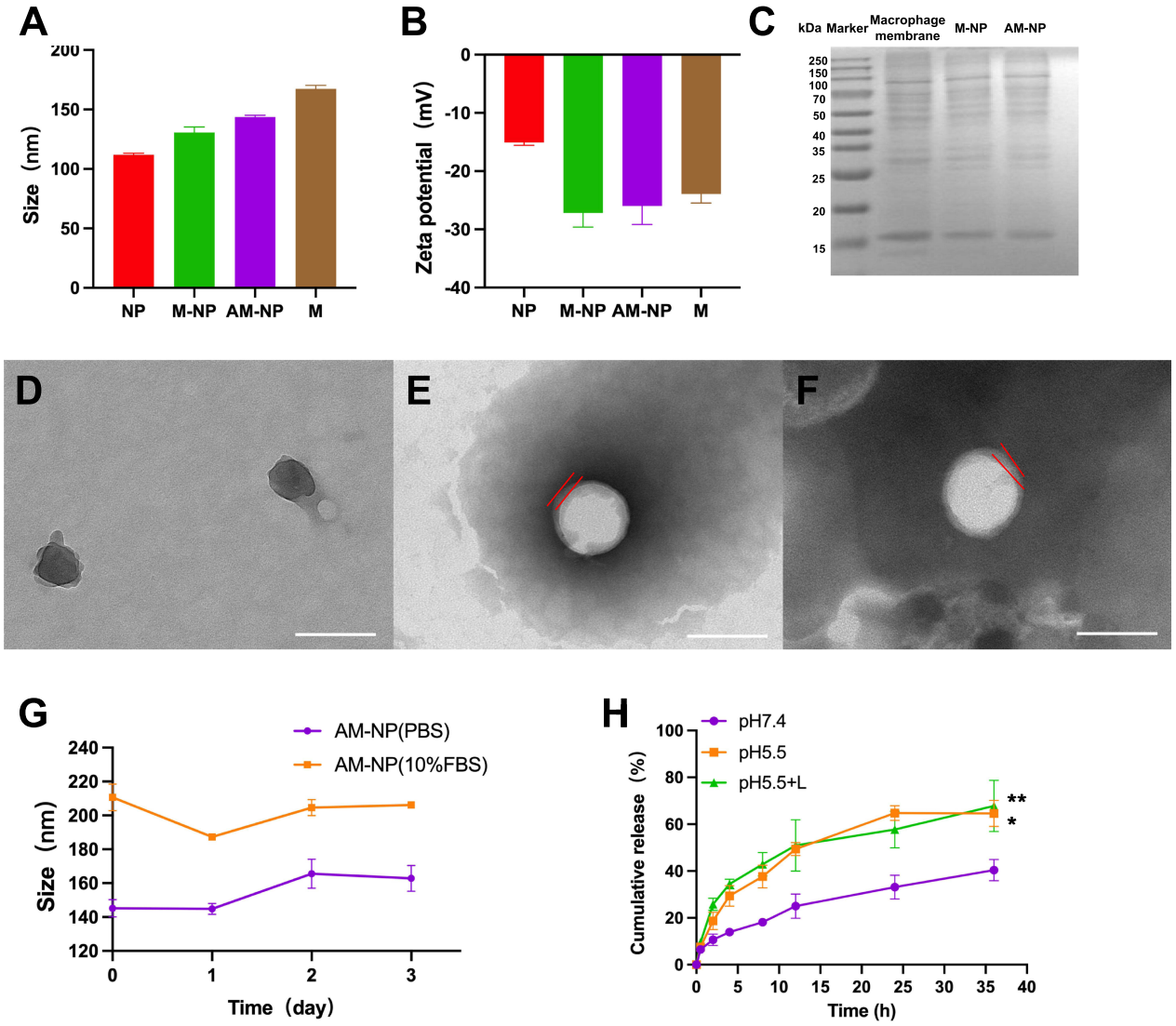

Figure 1 Preparation and characterization of fabricated nanoparticles. (**A** and **B**) Hydrodynamic size and zeta potential of different ICG formulations. (**C**) SDS-PAGE protein analysis of membrane only, M-NP and AM-NP. (**D**–**F**) TEM imaging of (**D**) NP, (**E**) M-NP, (**F**) AM-NP. Scale bars: 100 nm. (**G**) Long-term stability study of AM-NP in PBS and 10% FBS. (**H**) SN38 release profiles from AM-NP pH 7.4 or pH 5.5. (*p < 0.05,**p < 0.01).

concentration of 0.25 mg (Figure S3). Based on Figure 1A and B, during the preparation process from NP to AM-NP, the addition of macrophage membrane coating and Angiopep-2 modification led to a slight increase in the nanoparticles size. Meanwhile, the surface zeta potential of the nanoparticles gradually approached that of the macrophage membrane, indicating the successful construction of the biomimetic nano-platform. Subsequently, the membrane protein concentration extracted from macrophages was measured, and changes in the membrane protein composition after nanoparticle formation were verified through SDS-PAGE gel electrophoresis. As depicted in Figure 1C, the protein bands of M-NP and AM-NP closely resembled those of pure macrophage membrane proteins, indicating that the membrane-encapsulated nanoparticles we prepared retained the protein composition of macrophage membranes without altering their inherent functionality. Under transmission electron microscopy (TEM), nanoparticles were observed to exhibit a spherical morphology (Figure 1D–F), Simultaneously, both M-NP and AM-NP exhibit a distinct core-shell structure, with an outer cell membrane thickness of approximately 10 nm. This aligns well with the trend presented by the DLS measurement results. Interestingly, TEM images revealed that after laser irradiation, the diameter of the nanoparticles increased to 300–400 nm (Figure S4), indicating that light exposure caused a change in the nanoparticle structure, expanding their size to approximately three times their original size. The final prepared AM-NPs were dispersed in PBS

and 10% FBS, minimal changes in particle size were observed within three days (Figure 1G). Additionally, there were almost no changes in the zeta potential and TEM (Figure S5), indicating excellent stability.

Then we simulated physiological and tumor microenvironments at different pH values (5.5 and 7.4) to investigate the release behavior of SN38 from AM-NPs. As shown in Figure 1H, after incubation in PBS (pH 7.4) for 24 h, the cumulative release of SN38 reached 33.2±3.1%. During the same time period, under acidic conditions (pH 5.5), the release rate was faster, and the amount of released SN38 reached 64.7±3.4%. We attribute the accelerated release to the possibility that acidic conditions expedite cell membrane degradation and disrupt the self-assembled nanostructures' π-π stacking, leading to a faster drug release.[49,50] In the laser irradiation group, it was observed that within the first 12 h, accelerated nanoparticle decomposition due to light exposure led to a faster release of SN38. After 12 h, the release of SN38 gradually slowed down, with the final release effect slightly higher than the group that did not undergo laser irradiation.

Cellular Uptake

To verify that the prepared M-NP and AM-NP can enhance the uptake by tumor cells, GL261 cells were treated with three types of nanoparticles at the same concentration for 1 h and observed the cellular uptake under a fluorescence microscope. As shown in Figure 2A, cells treated with AM-NP exhibited a higher uptake capacity about 45% compared to the M-NP and NP groups. Quantitative analysis of fluorescence intensity using ImageJ yielded consistent conclusions

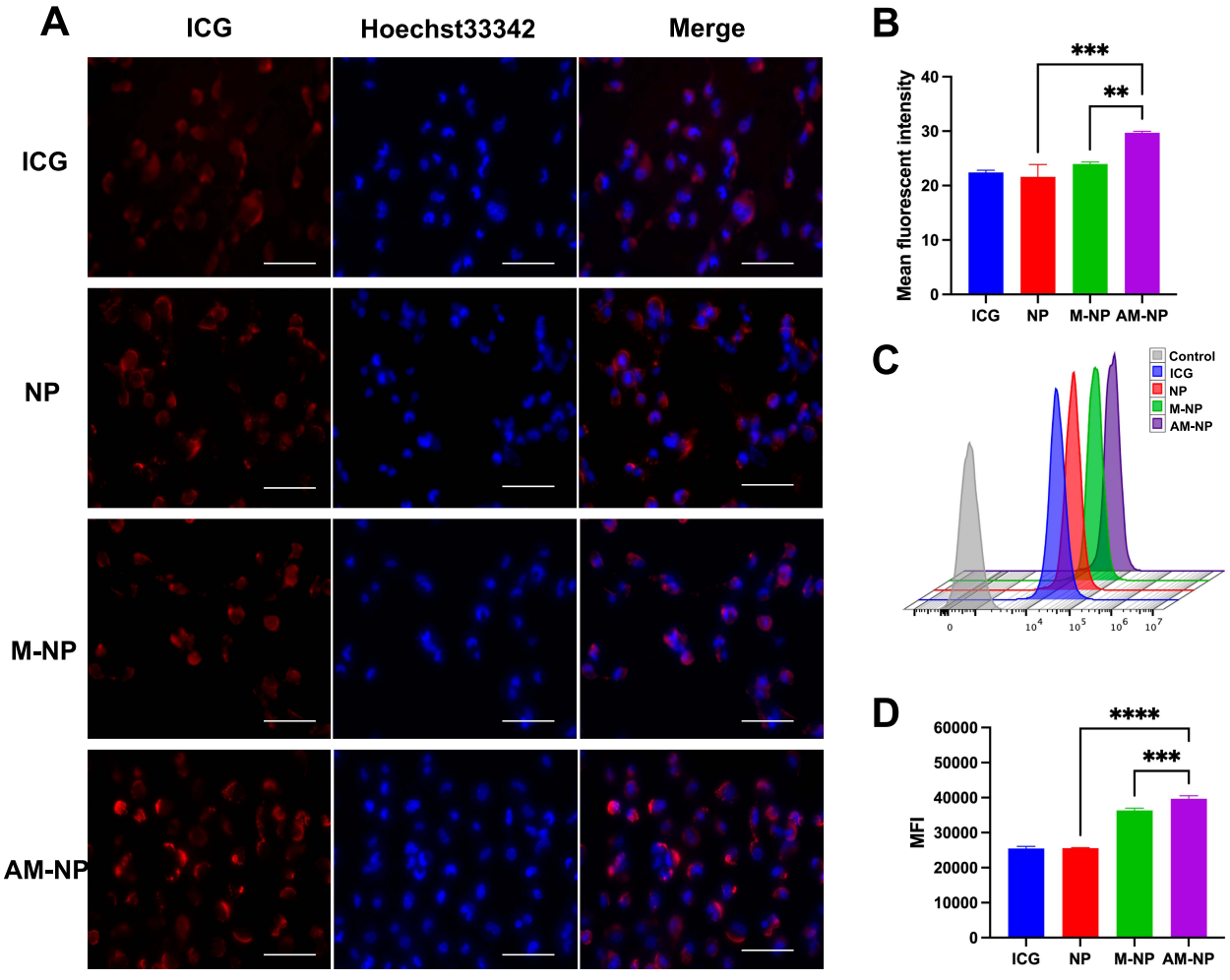

Figure 2 (**A**) Fluorescence images of cell uptake of ICG, NP, M-NP and AM-NP by fluorescence microscopy after 1 h of incubation with GL261 cells. Scale bars: 150 μm. (**B**) Qualitative results analyzed by ImageJ of cell uptake. (**p < 0.01, ***p < 0.001) (**C**) Cell uptake by flow cytometry: histogram of GL261 for different nanoparticle uptake. (**D**) Quantitative cellular uptake results were analyzed by flow cytometry. (***p < 0.001,****p < 0.0001).

(Figure 2B). Simultaneously, experimental results from the time gradient indicate that cells exhibit more complete drug uptake at 8 hours (Figure S6).

Furthermore, we conducted a quantitative study of cell uptake using flow cytometry. As illustrated in Figure 2C and D, compared to the M-NP and NP groups, AM-NP demonstrated a faster cellular uptake into GL261 cells mediated by surface-modified peptides. Simultaneously, the M-NP group without peptide modification also exhibited a superior uptake effect compared to NP. These results collectively indicate the successful surface modification of the membrane with Angiopep-2 peptide, facilitating the rapid infiltration of nanoparticles into tumor cells.

In competitive experiments, GL261 cells pre-treated with Angiopep-2 exhibited reduced uptake of AM-NP, whereas those without peptide pre-treatment showed bright fluorescence. This further confirms that Angiopep-2 can mediate the entry of nanoparticles into cells, enhancing uptake efficiency (Figure S7).

Subsequently, the effect of cell membrane-coated nanocarriers on evading clearance were examined using RAW264.7 cells. As shown in Figure S8, bright red fluorescence was observed in macrophages incubated with NP for 2 h. In contrast, AM-NP, modified with macrophage membrane, exhibited only weak fluorescence. This indicates that the biomimetic delivery system encapsulated by macrophage membrane can effectively evade macrophage clearance.

In vitro Cytotoxicity Studies and BBB Penetration

The cytotoxicity of different nanocarrier treatments combined with photothermal treatments was further evaluated. As shown in Figures 3A and S9, the cytotoxicity of the three formulations increased with the elevated concentration of SN38. Meanwhile, the results from the combined photothermal treatment group indicated that the photothermal effect of indocyanine green (ICG) was only observed when reaching a certain concentration. To validate this result, a comparative experiment was performed between free ICG and free ICG+laser treatment. The results demonstrated that the cell viability in the ICG+laser treatment group significantly decreased to below 10% at a concentration of 50 μM (Figure 3B). Additionally, experiments were conducted with a quantified concentration of 100 μM for ICG, and the results, as depicted in Figure 3C, showed that the cell survival rate after combined photothermal treatment was below 10%, further confirming the aforementioned conclusion. These results indicate significant inhibitory effects of the prepared nanocarriers on GL261 cells, and the combined photothermal therapy achieves a almost effective and thorough cell killing.

During the investigation of BBB permeability, we ensured that the transendothelial electrical resistance (TEER) remained above 80 $\Omega \cdot cm^{-2}$ to confirm the establishment of the BBB model (Figure S10). The results demonstrated that the ICG concentration in the lower layer of the AM-NP group was higher than that in the NP and MNP groups in Figure 3D, indicating that the surface modification of macrophage membranes with Angiopep-2 facilitated the transport of nanocarriers through binding to the overexpressed low-density lipoprotein receptors in the cells.

Cellular Uptake Pathways and Subcellular Distribution

Furthermore, to investigate through which endocytic pathway BBB penetration is achieved, flow cytometry analysis revealed that pre-treatment with macropinocytosis and clathrin channel inhibitors resulted in approximately a 30% reduction in bEnd.3 cell uptake of nanoparticles (Figure S11). This suggests that AM-NP may be internalized by cells and penetrate the BBB through macropinocytosis and clathrin-mediated endocytosis. In the co-localization study (Figure S12), it was observed that after 4 h of cell uptake, AM-NP had already escaped from the lysosomes and entered the cytoplasm, and exert its activity.

Inhibition and Penetration Ability of Nanoparticles on Tumor Spheroids

Tumor spheroids were further constructed to validate the anti-tumor capability of the nanocarrier in combination with photothermal therapy. As illustrated in Figure 3E and F, the control group without drug treatment exhibited rapid tumor spheroid growth, reaching more than twice the original volume by the fifth day. By contrast, the AM-NP-treated group effectively suppressed the growth of tumor spheroids, with the morphology gradually transitioning to a dispersed state in the later stages. The AM-NP+laser group demonstrated the most favorable therapeutic outcome, with the tumor spheroid volume showing little change compared to the initial state. This indicates that the combination of AM-NP and photothermal therapy can effectively inhibit tumor spheroids growth.

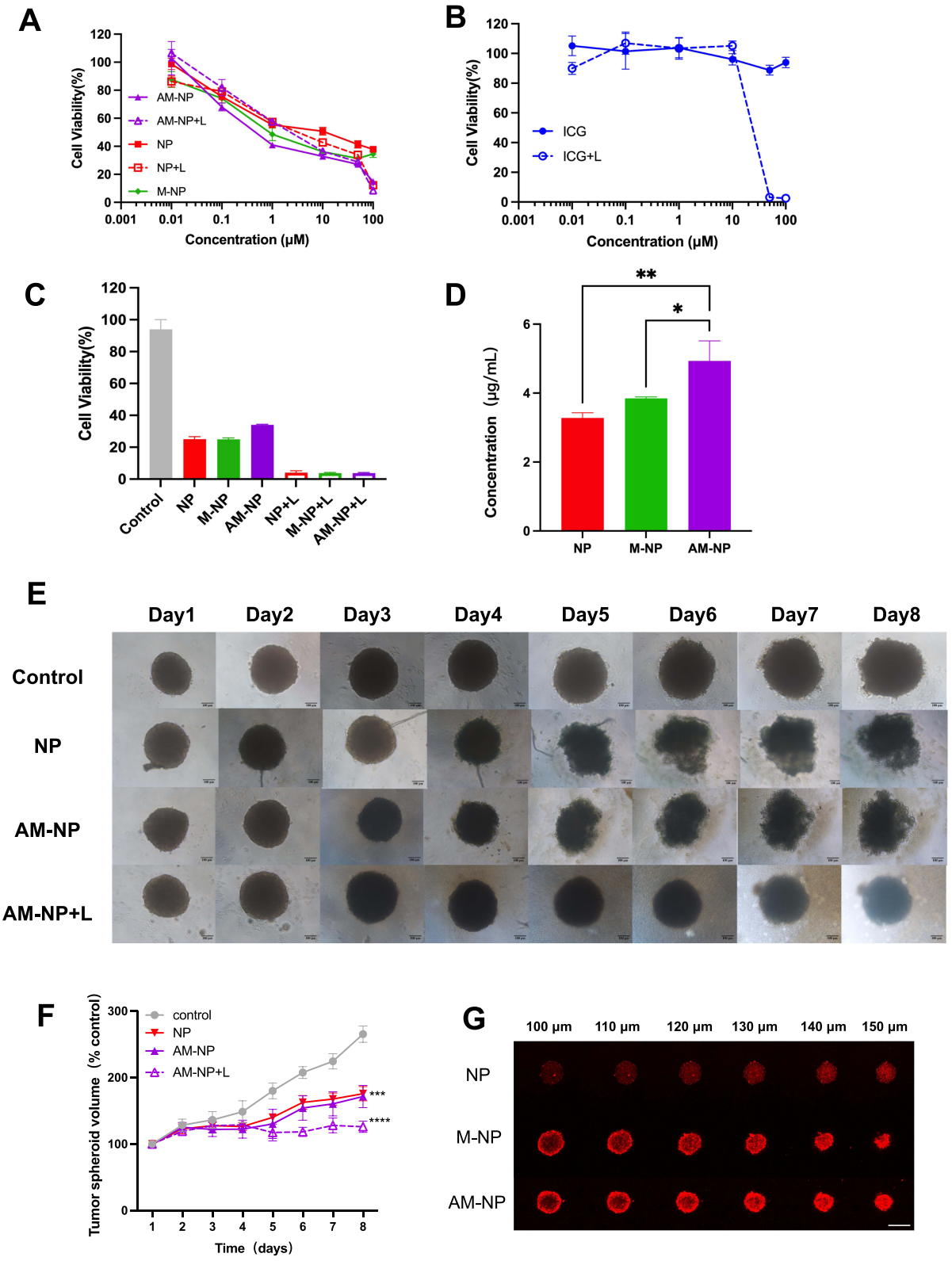

Figure 3 In vitro cytotoxicity of fabricated nanoparticles in both cells and spheroids model. (**A** and **B**) Cytotoxicity assay of different ICG formulations in GL261 cells in vitro (**C**) Cell viability assayed at an ICG of 100 μM (SN38: 20 μg/mL) (**D**) Transcytosis ability of different ICG formulations. (*p < 0.05,**p < 0.01) (**E**) The inhibitory ability of different nanoparticles on GL261 3D spheroids. (**F**) Volume changes of 3D spheroids under different treatments. (**G**) Permeation of different nanoparticles in 3D spheroids. Scale bar: 200 μm.

To further assess the penetration capability of the nanocarrier within tumor spheroids, GL261 cell tumor spheroids were constructed for penetration experiments. As shown in Figure 3G, compared to the NP group, both M-NP and AM-NP exhibited intense red fluorescence, especially the AM-NP treated group demonstrating a more concentrated uptake indicating the spheres penetrated deeper due to the peptide target ability and membrane's dual target and penetration ability.

In vitro ICD Effects

ATP secretion and calreticulin (CRT) exposure are two crucial indicators of immunogenic cell death (ICD).[51,52] Calreticulin (CRT), a multifunctional protein located in the endoplasmic reticulum, is exposed on the cell membrane surface during ICD. As shown in Figure S13, both the control and ICG groups exhibit no green fluorescence labeled by antibodies, whereas the ICG+L group shows faint green fluorescence. In contrast, cells in the AM-NP+L group emit intense fluorescence on the cell membrane surface, indicating the induction of ICD through photothermal treatment, leading to the externalization of CRT.

As depicted in Figure S14, the ATP secretion levels in the ICG+L and AM-NP+L groups are significantly higher than those in the non-irradiated group. This indicates that the combined photothermal treatment enhances ATP release, effectively inducing immunogenic cell death in tumor cells.

In vivo Pharmacokinetics

As shown in Figure 4B and Table 1, CPT-11 was rapidly cleared from the bloodstream. In contrast, both NP and AM-NP exhibit prolonged circulation times, the clearance half-life of the AM-NP group was 5.278 h, which was more than twice that of the CPT-11 group. This trend was also reflected in the area under the blood drug concentration-time curve. The data from the AM-NP group demonstrates an extended presence attributed to the "camouflage" effect of macrophage membrane coating and surface peptide modifications. These features attenuate blood clearance to a certain extent, facilitating enhanced accumulation of the drug at the tumor site.

In vivo Brain Tumor Targeting Ability Evaluation

As illustrated in Figure 4C, 2 hours post intravenous injection of nanoparticles, the fluorescence intensity in the brain region of the AM-NP group was notably higher than that of the NP group. After 8 hours of injection, whole-brain imaging was performed on mice. Ex vivo imaging results showed that the fluorescence in the AM-NP group was concentrated at the site where the tumor was inoculated on the right side, and the fluorescence signal was significantly higher compared to the NP group. In off-target organ accumulation, fluorescence signals primarily concentrated in the liver and kidneys, with the NP group showing higher accumulation in these organs. These findings indicate that the prepared AM-NP effectively targets the site of the brain tumor, leading to enhanced drug accumulation in the brain.

In vivo Antitumor Activity and Safety Study

A glioma orthotopic model was established to investigate the in vivo anti-tumor efficacy of nanocarriers (Figure S15). As illustrated in Figure 4D, within six days of GL261 cell inoculation, all groups of mice experienced a period of weight gain. After six days, the mice's weight began to decrease, and their physical condition gradually deteriorated. Specifically, the PBS group exhibited a rapid decline in weight, while the weight reduction in the AM-NP+L group was relatively slower compared to other groups of mice. The survival period of mice, as depicted in Figure 4E, revealed a significant extension in the median survival period for the AM-NP+L group of about 7 days. This can be attributed to the strong brain-targeting ability of AM-NP, allowing the drug to accumulate at the tumor site, thereby further enhancing the synergistic anti-tumor effect of photothermal therapy. Importantly, both NP and AM-NP mediated photothermal effects, with the AM-NP+L group demonstrating a stronger photothermal effect. As shown in Figure 4F, the tumor site temperature in the AM-NP+L group increased to 48.6°C after 2 min of 808 nm laser irradiation, surpassing the efficacy of the NP group at 43.1°C.

After three rounds of administration, two mice from each group were randomly euthanized, and their brains and other organs were collected for hematoxylin and eosin (H&E) staining analysis. As shown in Figure 4G, the brains of the mice

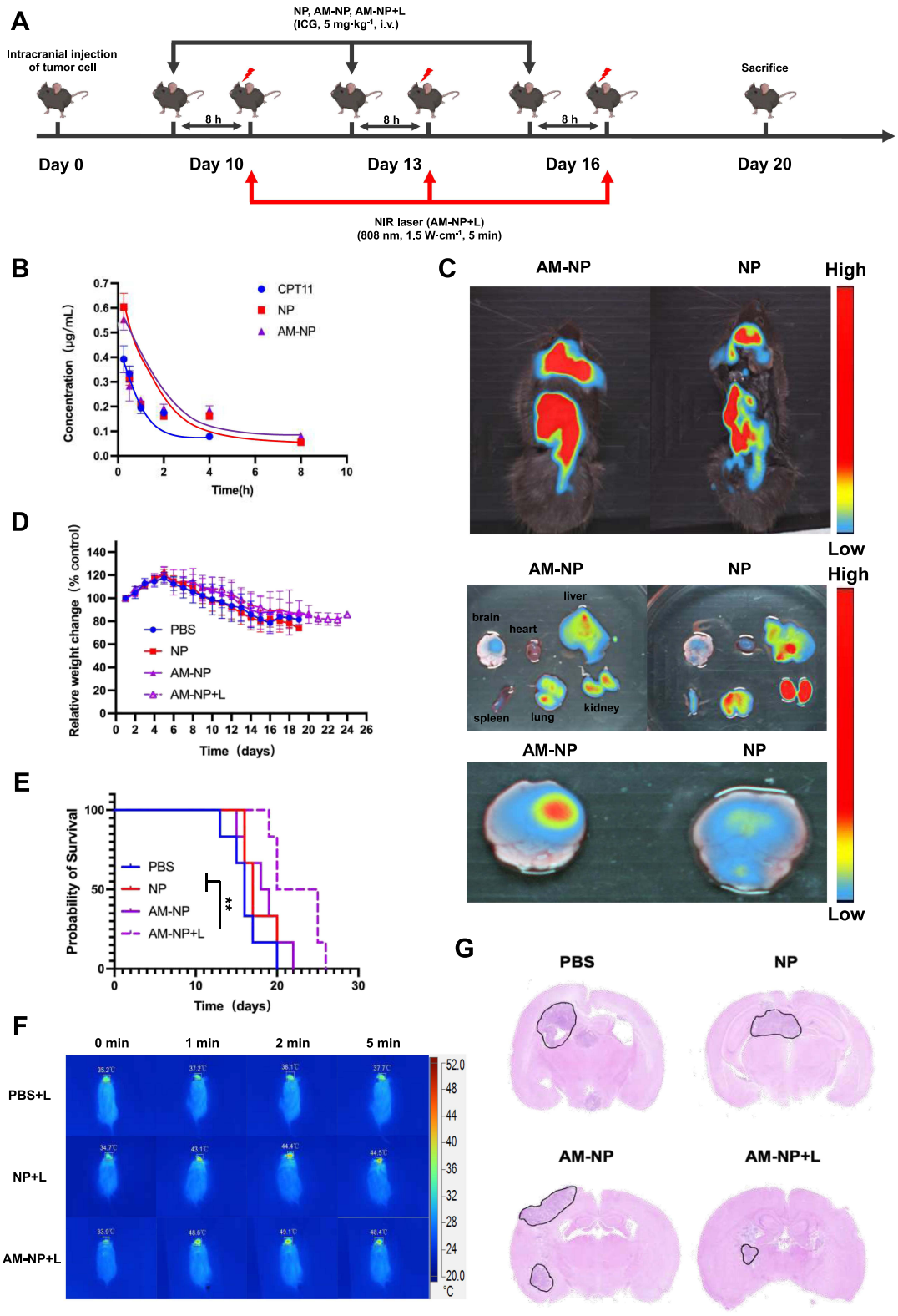

Figure 4 (**A**) Schematic diagram of in vivo therapy. (**B**) Concentration of SN-38 in mice plasma after tail vein injection of different formulations. (n=6, at the dose of SN-38 5 mg/kg). (**C**) In vivo imaging of orthotopic glioma models of mice treated with different formulations after 2 h and ex vivo imaging of mouse organs after injection with different formulations for 8 h. (**D**) The body weight changes of mice after implantation. (**E**) Survival curve of mice after administration by tail vein injection (n=6, at the dose of SN-38 5 mg/kg, **p < 0.01). (**F**) Representative in vivo infrared thermal images of mice before and after 808 nm laser irradiation (1.5 W·cm^{-2}, 5 min). (**G**) H&E imaging of brain sections from different treatment groups. (The black underlined part was the tumor area).

Table 1 Pharmacokinetic Parameters of Mice I.v. Injected with 5 mg·Kg^{-1} of Nanoparticles

Parameters	CPT-11	NP	AM-NP
C_{max} (mg·L^{-1})	0.449	0.667	0.584
$t_{1/2\alpha}$ (h)	0.195	0.106	0.066
$t_{1/2\beta}$ (h)	2.254	4.055	5.278
AUC $_{(0-\infty)}$(mg·L^{-1}·h^{-1})	0.978	1.491	2.271
CL (L·h^{-1}·kg^{-1})	5.114	3.199	2.202

Abbreviations: C_{max}, Peak Plasma Concentration; $t_{1/2\alpha}$, distribution half-life; $t_{1/2\beta}$, elimination half-life; AUC $_{(0-\infty)}$, area under curve; CL, plasma clearance.

exhibited clear evidence of tumor infiltration, displaying a progressively invasive growth pattern that spread throughout the entire brain. Notably, the tumor area in the AM-NP+L group was relatively smaller, consistent with a favorable anti-tumor effect observed in the experiment. Safety analyses were concurrently conducted on other tissues, as depicted in Figure 5. H&E staining results of the heart, liver, spleen, lung, and kidney demonstrate distinct tissue characteristics. In heart sections, cardiomyocytes exhibit clear striations with centrally located nuclei, and vascular distribution is observed in the intercellular matrix, maintaining normal structural features. Liver sections display hepatocytes arranged in cords around the central vein, forming hepatic cell plates with visible hepatic sinusoids, consistent with typical liver tissue architecture. Both white and red pulp are clearly visible in spleen sections, representing normal spleen structure. Lung tissue sections exhibit clear and intact alveolar structures without apparent lesions or abnormalities. Kidney tissue sections show no dilation or obstruction. Simultaneously, as shown in Figure S16, TUNEL staining of normal brain

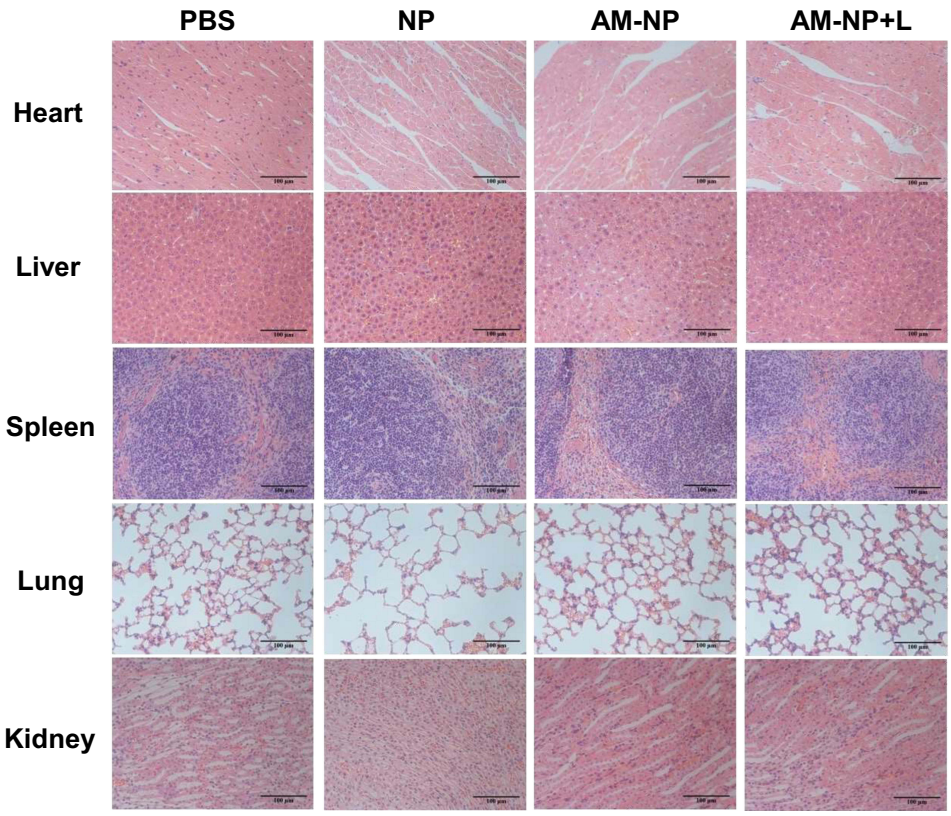

Figure 5 H&E stained sections of the major organs of mice treated with different nanoparticles. (n=6, at the dose of SN-38 5 mg/kg).

tissue regions revealed no occurrence of apoptosis. These observations collectively suggest that the nanoparticles used possess excellent biocompatibility.

Conclusion

To maintain an effective drug concentration in deep tumor lesions remains an unsurmountable challenge in GBM treatment. This study developed biomimetic nanoparticles, termed AM-NP, with the capability to penetrate the blood-brain barrier and target the tumor cells. These nanoparticles are based on the high affinity of Angiopep-2 for low-density lipoprotein receptors and the specific binding of macrophage cells to integrin receptors, achieving a dual-targeting strategy for glioblastomas. Upon achieving high drug accumulation at the tumor site, ICG-induced photothermal therapy rapidly increases temperature to suppress tumor growth, while SN38 further releases to facilitate chemotherapy, ultimately achieving a synergistic chemo-photothermal treatment. In comparison to bare nanoparticles (NP) without cell membrane coating, AM-NP effectively inhibited tumor growth and significantly prolonged the survival of mice, with excellent biocompatibility and minimal side effects. These findings present a novel strategy for precise targeting and multimodal treatment of glioblastomas.

Ethics Approval and Informed Consent

All experimental procedures involving animals were ethically approved by the Animal Ethics Committee of Zhejiang University of Technology and conducted in strict adherence to the Guidelines for the Care and Use of Laboratory Animals of Zhejiang University of Technology.

Acknowledgment

We sincerely thank Prof. Jing Yu and Dr. Fan Zhao for technical support of ICG.

Funding

This project was supported by the National Natural Science Foundation of China (No.22075247), the Zhejiang Provincial Natural Science Foundation of China (No. LGF21C100001), the China Postdoctoral Science Foundation (No. 2023M743104), and the Postdoctoral Fellowship Program of CPSF (No. GZC20232365), Zhejiang Provincial Key Laboratory of TCM for Innovative R&D and Digital Intelligent Manufacturing of TCM Great Health Products and Key Research and Development Program of Zhejiang Province (No.2021C03084).

Disclosure

The authors declare no competing interests in this work.

References

1. Qiao C, Zhang R, Wang Y, et al. Rabies virus-inspired Metal-Organic Frameworks (MOFs) for targeted imaging and chemotherapy of glioma. Article. *Angew Chem*. 2020;59(39):16982–16988. doi:10.1002/anie.202007474
2. Hu H, Mu Q, Bao Z, et al. Mutational landscape of secondary glioblastoma guides MET-targeted trial in brain tumor. Article. *Cell*. 2018;175(6):1665–+. doi:10.1016/j.cell.2018.09.038
3. Cuddapah VA, Robel S, Watkins S, Sontheimer H. A neurocentric perspective on glioma invasion. *Nat Rev Neurosci*. 2014;15(7):455–465. doi:10.1038/nrn3765
4. Parney IF, Chang SM. Current chemotherapy for glioblastoma. *Cancer J*. 2003;9(3):149–156. doi:10.1097/00130404-200305000-00003
5. Lieberman F. Glioblastoma update: molecular biology, diagnosis, treatment, response assessment, and translational clinical trials. *F1000Res*. 2017;6:1892. doi:10.12688/f1000research.11493.1
6. Thakkar JP, Dolecek TA, Horbinski C, et al. Epidemiologic and molecular prognostic review of glioblastoma. *Cancer Epidemiol Biomarkers Prev*. 2014;23(10):1985–1996. doi:10.1158/1055-9965.EPI-14-0275
7. Li X, Geng X, Chen Z, Yuan Z. Recent advances in glioma microenvironment-response nanoplatforms for phototherapy and sonotherapy. *Pharmacol Res*. 2022;179:106218. doi:10.1016/j.phrs.2022.106218
8. Brown JM, Recht L, Strober S. The promise of targeting macrophages in cancer therapy. *Clin Cancer Res*. 2017;23(13):3241–3250. doi:10.1158/1078-0432.CCR-16-3122
9. Buerki RA, Chheda ZS, Okada H. Immunotherapy of primary brain tumors: facts and hopes. *Clin Cancer Res*. 2018;24(21):5198–5205. doi:10.1158/1078-0432.CCR-17-2769

10. Hanif S, Muhammad P, Niu Z, et al. Nanotechnology-based strategies for early diagnosis of central nervous system disorders. *Adv Nano Biomed Res*. 2021;1(10). doi:10.1002/anbr.202100008
11. Muhammad P, Hanif S, Li J, et al. Carbon dots supported single Fe atom nanozyme for drug-resistant glioblastoma therapy by activating autophagy-lysosome pathway. *Nano Today*. 2022;45:101530. doi:10.1016/j.nantod.2022.101530
12. van Solinge TS, Nieland L, Chiocca EA, Broekman MLD. Advances in local therapy for glioblastoma - taking the fight to the tumour. *Nat Rev Neurol*. 2022;18(4):221–236. doi:10.1038/s41582-022-00621-0
13. Yan J, Hanif S, Zhang D, et al. Arsenic prodrug-mediated tumor microenvironment modulation platform for synergetic glioblastoma therapy. *ACS Appl Mater Interfaces*. 2022;14(32):36487–36502. doi:10.1021/acsami.2c12076
14. Mitusova K, Peltek OO, Karpov TE, Muslimov AR, Zyuzin MV, Timin AS. Overcoming the blood-brain barrier for the therapy of malignant brain tumor: current status and prospects of drug delivery approaches. *J Nanobiotechnol*. 2022;20(1):412. doi:10.1186/s12951-022-01610-7
15. Habashy KJ, Dmello C, Chen L, et al. Paclitaxel and carboplatin in combination with low-intensity pulsed ultrasound for glioblastoma. *Clin Cancer Res*. 2024;30(8):1619–1629. doi:10.1158/1078-0432.CCR-23-2367
16. Schoen S Jr, Kilinc MS, Lee H, et al. Towards controlled drug delivery in brain tumors with microbubble-enhanced focused ultrasound. *Adv Drug Deliv Rev*. 2022;180:114043. doi:10.1016/j.addr.2021.114043
17. Xu YY, Gao P, Sun Y, Duan YR. Development of targeted therapies in treatment of glioblastoma. *Cancer Biol Med*. 2015;12(3):223–237. doi:10.7497/j.issn.2095-3941.2015.0020
18. Guo QL, Dai XL, Yin MY, et al. Nanosensitizers for sonodynamic therapy for glioblastoma multiforme: current progress and future perspectives. *Military Med Res*. 2022;9(1). doi:10.1186/s40779-022-00386-z
19. Bai L, Liu Y, Guo K, et al. Ultrasound facilitates naturally equipped exosomes derived from macrophages and blood serum for orthotopic glioma treatment. *ACS Appl Mater Interfaces*. 2019;11(16):14576–14587. doi:10.1021/acsami.9b00893
20. Park J, Aryal M, Vykhodtseva N, Zhang YZ, McDannold N. Evaluation of permeability, doxorubicin delivery, and drug retention in a rat brain tumor model after ultrasound-induced blood-tumor barrier disruption. *J Control Release*. 2017;250:77–85. doi:10.1016/j.jconrel.2016.10.011
21. Rehman FU, Rauf MA, Ullah S, et al. Ultrasound-activated nano-TiO2 loaded with temozolomide paves the way for resection of chemoresistant glioblastoma multiforme. *Cancer Nanotechnol*. 2021;12(1). doi:10.1186/s12645-021-00088-6
22. Foley CP, Rubin DG, Santillan A, et al. Intra-arterial delivery of AAV vectors to the mouse brain after mannitol mediated blood brain barrier disruption. *J Control Release*. 2014;196:71–78. doi:10.1016/j.jconrel.2014.09.018
23. Rapoport SI. Osmotic opening of the blood-brain barrier: principles, mechanism, and therapeutic applications. *Cell Mol Neurobiol*. 2000;20 (2):217–230. doi:10.1023/a:1007049806660
24. Xue J, Zhao Z, Zhang L, et al. Neutrophil-mediated anticancer drug delivery for suppression of postoperative malignant glioma recurrence. *Nat Nanotechnol*. 2017;12(7):692–700. doi:10.1038/nnano.2017.54
25. Israel LL, Galstyan A, Holler E, Ljubimova JY. Magnetic iron oxide nanoparticles for imaging, targeting and treatment of primary and metastatic tumors of the brain. *J Control Release*. 2020;320:45–62. doi:10.1016/j.jconrel.2020.01.009
26. Wu M, Zhang H, Tie C, et al. MR imaging tracking of inflammation-activatable engineered neutrophils for targeted therapy of surgically treated glioma. *Nat Commun*. 2018;9(1):4777. doi:10.1038/s41467-018-07250-6
27. Wang M, Lv CY, Li SA, et al. Near infrared light fluorescence imaging-guided biomimetic nanoparticles of extracellular vesicles deliver indocyanine green and paclitaxel for hyperthermia combined with chemotherapy against glioma. *J Nanobiotechnol*. 2021;19(1):210. doi:10.1186/s12951-021-00907-3
28. Rufino-Ramos D, Albuquerque PR, Carmona V, Perfeito R, Nobre RJ, Pereira de Almeida L. Extracellular vesicles: novel promising delivery systems for therapy of brain diseases. *J Control Release*. 2017;262:247–258. doi:10.1016/j.jconrel.2017.07.001
29. Fang RH, Hu CM, Luk BT, et al. Cancer cell membrane-coated nanoparticles for anticancer vaccination and drug delivery. *Nano Lett*. 2014;14 (4):2181–2188. doi:10.1021/nl500618u
30. Chen Z, Zhao P, Luo Z, et al. Cancer cell membrane-biomimetic nanoparticles for homologous-targeting dual-modal imaging and photothermal therapy. *ACS Nano*. 2016;10(11):10049–10057. doi:10.1021/acsnano.6b04695
31. Ismail M, Yang W, Li Y, et al. Biomimetic Dp44mT-nanoparticles selectively induce apoptosis in Cu-loaded glioblastoma resulting in potent growth inhibition. *Biomaterials*. 2022;289:121760. doi:10.1016/j.biomaterials.2022.121760
32. Chen H, Li T, Liu Z, et al. A nitric-oxide driven chemotactic nanomotor for enhanced immunotherapy of glioblastoma. *Nat Commun*. 2023;14 (1):941. doi:10.1038/s41467-022-35709-0
33. Quader S, Kataoka K, Cabral H. Nanomedicine for brain cancer. *Adv Drug Deliv Rev*. 2022;182:114115. doi:10.1016/j.addr.2022.114115
34. Tseng YY, Yang TC, Chen SM, Yang ST, Tang YL, Liu SJ. Injectable SN-38-embedded polymeric microparticles promote antitumor efficacy against malignant glioma in an animal model. *Pharmaceutics*. 2020;12(5). doi:10.3390/pharmaceutics12050479
35. Gao HL. Progress and perspectives on targeting nanoparticles for brain drug delivery. *Acta Pharm Sin B*. 2016;6(4):268–286. doi:10.1016/j.apsb.2016.05.013
36. Tammam SN, Azzazy HME, Lamprecht A. Nuclear and cytoplasmic delivery of lactoferrin in glioma using chitosan nanoparticles: cellular location dependent-action of lactoferrin. *Eur J Pharm Biopharm*. 2018;129:74–79. doi:10.1016/j.ejpb.2018.05.027
37. Pulgar VM. Transcytosis to cross the blood brain barrier, new advancements and challenges. *Front Neurosci*. 2018;12:1019. doi:10.3389/fnins.2018.01019
38. Gordon S, Taylor PR. Monocyte and macrophage heterogeneity. *Nat Rev Immunol*. 2005;5(12):953–964. doi:10.1038/nri1733
39. Noy R, Pollard JW. Tumor-associated macrophages: from mechanisms to therapy. *Immunity*. 2014;41(1):49–61. doi:10.1016/j.immuni.2014.06.010
40. Quail DF, Joyce JA. Microenvironmental regulation of tumor progression and metastasis. *Nat Med*. 2013;19(11):1423–1437. doi:10.1038/nm.3394
41. Song W, Zhang X, Song Y, et al. Enhancing photothermal therapy efficacy by in situ self-assembly in glioma. *ACS Appl Mater Interfaces*. 2023;15 (1):57–66. doi:10.1021/acsami.2c14413
42. Zhang X, He Z. Cell membrane coated pH-responsive intelligent bionic delivery nanoplatform for active targeting in photothermal therapy. *Int J Nanomed*. 2023;18:7729–7744. doi:10.2147/IJN.S436940
43. Gao C, Huang Q, Liu C, et al. Treatment of atherosclerosis by macrophage-biomimetic nanoparticles via targeted pharmacotherapy and sequestration of proinflammatory cytokines. Article. *Nat Commun*. 2020;11(1). doi:10.1038/s41467-020-16439-7

44. Cao H, Dan Z, He X, et al. Liposomes coated with isolated macrophage membrane can target lung metastasis of breast cancer. *ACS Nano*. 2016;10(8):7738–7748. doi:10.1021/acsnano.6b03148
45. Hu S, Dong C, Wang J, et al. Assemblies of indocyanine green and chemotherapeutic drug to cure established tumors by synergistic chemo-photo therapy. *J Control Release*. 2020;324:250–259. doi:10.1016/j.jconrel.2020.05.018
46. Chi SY, Zhang L, Cheng HM, et al. Biomimetic nanocomposites camouflaged with hybrid cell membranes for accurate therapy of early-stage glioma. *Angew Chem*. 2023;62(29). doi:10.1002/anie.202304419
47. Liu Y, Hu DH, Gao DY, et al. Engineered apoptotic bodies hitchhiking across the blood-brain barrier achieved a combined photothermal-chemotherapeutic effect against glioma. *Theranostics*. 2023;13(9):2966–2978. doi:10.7150/thno.80632
48. Jia YL, Wang XB, Hu DH, et al. Phototheranostics: active targeting of orthotopic glioma using biomimetic proteolipid nanoparticles (vol 13, pg 386, 2019). *Acs Nano*. 2021;15(6):10733. doi:10.1021/acsnano.1c04547
49. Lin J, Li C, Guo Y, et al. Carrier-free nanodrugs for in vivo NIR bioimaging and chemo-photothermal synergistic therapy. *J Mater Chem B*. 2019;7(44):6914–6923. doi:10.1039/c9tb00687g
50. Kang B, Li J, Chang S, et al. Subcellular tracking of drug release from carbon nanotube vehicles in living cells. *Small*. 2012;8(5):777–782. doi:10.1002/smll.201101714
51. Park W, Wei S, Kim BS, et al. Diversity and complexity of cell death: a historical review. *Exp Mol Med*. 2023;55(8):1573–1594. doi:10.1038/s12276-023-01078-x
52. Zhang L, Montesdeoca N, Karges J, Xiao H. Immunogenic cell death inducing metal complexes for cancer therapy. *Angew Chem Int Ed Engl*. 2023;62(21):e202300662. doi:10.1002/anie.202300662